Ferromagnetic resonance in a topographically modulated permalloy film

J. Sklenar,[1] P. Tucciarone,[2] R. J. Lee,[1] D. Tice,[3] R. P. H. Chang,[4]

S. J. Lee,[5] I. P. Nevirkovets,[1] O. Heinonen,[6,1] and J. B. Ketterson[1,7]

[1]*Department of Physics and Astronomy, Northwestern University, Evanston IL, 60208*

[2]*Department of Chemical and Biological Engineering,*

University at Buffalo (SUNY), Buffalo, New York 14260

[3]*Department of Chemistry, Northwestern University, Evanston IL, 60208*

[4]*Department of Materials Science and Engineering,*

Northwestern University, Evanston IL, 60208

[5]*Department of Physics, Hanyang University, Seoul 133-791, South Korea*

[6]*Materials Science Division, Argonne National Laboratory Argonne IL, 60439*

[7]*Department of Electrical and Computer Engineering,*

Northwestern University, Evanston IL, 60515

Abstract

A major focus within the field of magnonics involves the manipulation and control of spin wave modes. This is usually done by patterning continuous soft magnetic films. Here, we report on work in which we use topographic modifications of a continuous magnetic thin film, rather than lithographic patterning techniques, to modify the ferromagnetic resonance spectrum. To demonstrate this technique we have performed in-plane, broad-band, ferromagnetic resonance studies on a 100 nm thick Permalloy film sputtered unto a colloidal crystal with individual sphere diameters of 200 nm. Effects resulting from the, ideally, six-fold symmetric underlying colloidal crystal were studied as a function of the in plane field angle through experiment and micromagnetic modeling. Experimentally, we find two primary modes; the ratio of the intensities of these two modes exhibits a six-fold dependence. Detailed micromagnetic modeling shows that both modes are quasi-uniform and nodeless in the unit cell but that they reside in different demagnetized regions of the unit cell. Our results demonstrate that topographic modification of magnetic thin films opens new directions for manipulating ferromagnetic resonant excitations.

The phenomenon of ferromagnetic resonance (FMR) has been widely used to study the dynamic properties of magnetic nanostructures. The fabrication technique most commonly used is lithography, which can be expensive, and is limited by the available lithographic resolution; furthermore, producing topography introduces additional difficulties, even though some very intricate and complex structures – with very complex dynamics – have been produced[1]. Nevertheless, tailoring of magnetic films through lithographic means has revealed a host of interesting effects associated with the dynamic properties of these structures. In periodically patterned continuous structures spin wave control is realizable and has been paramount in the field of magnonics; this has been recently reviewed[2]. In contrast, isolated structures, like discs, harbor unique magnetic modes from single magnetic domain confinement[3]. An example of a confined mode is a vortex mode within an individual magnetic disc. The excitation of associated vortex modes have been exploited to change the vortex state of the disc[4] . More recently, FMR has been proposed as a tool to study geometric frustration in periodically patterned artificial spin ice structures[5]. The varying scope in these works is owed to the fact that much of the physics arises from geometrical demagnetization defined by the sample fabrication.

In this work we have studied how topography can modify the FMR spectrum of a permalloy (Py) film deposited on a colloidal crystal. To create this sample we have sputtered a Py film directly on top of a colloidal crystal, a self-assembled hexagonal close packed (HCP) array of polystyrene spheres. Compared to lithographically defined samples, far less work has been done using this approach. The geometrical details of these structures are not easily reproduced through lithography and, depending on the colloid diameter, small distance scales are readily achievable. Thus far the magneto-optical properties of magnetic films on colloidal crystals have been investigated[6]. Following this initial work there has been interest in geometrical frustration being built into such nanostructures[7–9]. In those works the frustration originated from the remanent state vortex on a given dome being unable to satisfy all it's nearest-neighbor interactions with other vortices within the HCP lattice. In lithographically defined samples there is a precedent to investigate, via FMR, structures that support vortices as they are a hotbed for new modes of excitation. Yet, for our topographically modified system no ferromagnetic resonance study has been performed. We do note that work has been done on inverse-opal structures that utilize colloidal crystals as a template of sorts[10].

The colloidal crystals serving as templates for our magnetic films are made from 200 nm diameter polystyrene spheres. Synthesis was accomplished using the well-known vertical deposition method[11]. Here, the lower part of a glass slide is immersed in a vial containing a solution of spheres in deionized water. The vial is placed within an oven and the water is allowed to evaporate. Crystal growth occurs at the evaporation line where the water meniscus contacts the glass slide. Our samples are single crystal over approximately a 1×1 cm^2 area. The colloidal crystal orientation has been verified to be preserved across this entire area by imaging different regions across the sample to check for rotations of the lattice vectors.
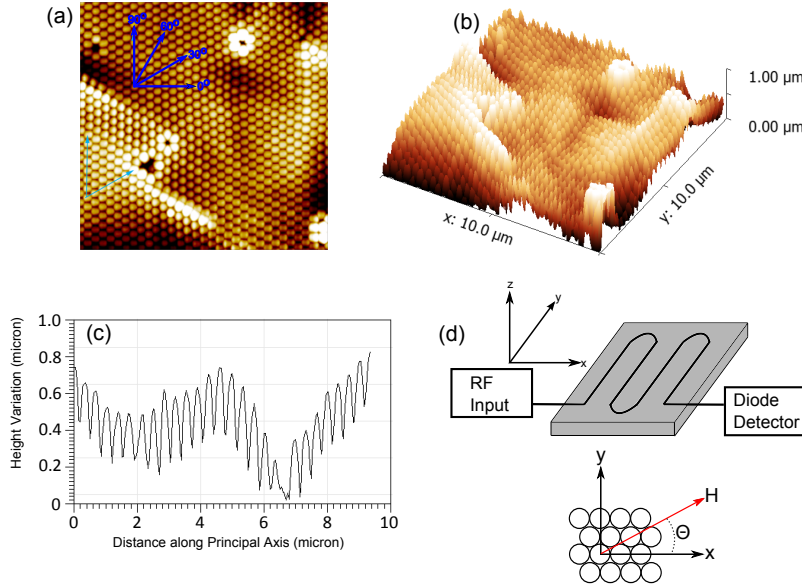
Figure 1. (a) is an AFM image of the colloidal crystal after Py sputtering; (b) shows the topographical uniformity of the resulting structure and commonly observed crystal defects; (c) is the height variation of the structure along one of the lattice vectors. The grey slab in the top inset of (d) is a representation of the sample. The black winding wire indicates, schematically the meanderline through which r passes; the turn spacing is close to 2 mm. The meanderline and sample lie in the XY plane and the field angle is measured off of the x-axis. The (100) crystal lattice direction lies along the x-axis.

After the crystals are fabricated, 40 nm of Ag followed by 100 nm of Py is sputtered onto the sample. The resulting structure can be seen in Fig. 1. In Fig. 1 (a) a top down AFM image clearly shows the HCP structure and six-fold symmetry. Some crystal defects, vacancies, and line defects are also seen. Additionally, the absolute height can change because the number of stacked spheres beneath the Py film can vary. An AFM-extracted topographical map (of the same region) is shown in Fig. 1 (b); part (c) shows a one dimensional cut with the height variation along a lattice vector.

To excite ferromagnetic resonance over a large area of the sample we utilize a meanderline technique[12]. Here we press a serpentine Cu wire over the surface of the Py film as shown in Fig. 1 (d). The microwaves pass through the meanderline and a ground plane lies beneath the sample. The output signal from the meanderline is rectified by a microwave diode and sent to a lock-in amplifier. During experiments we fix an excitation frequency of 10 GHz at 10 dBm (not including line losses) and sweep the magnetic field looking for microwave absorption as we modulate the magnetic field with a 40 Hz, 20 G RMS, AC magnetic field. For the experiments presented here we keep the magnetic field in the plane of the sample and rotate the in-plane field angle. The in-plane field angle with reference to the colloidal crystal crystalline axes is shown in Fig. 1 (d). When the in-plane field angle is 0° we expect the meanderline to have the weakest coupling to FMR because a significant portion of the exciting field will be parallel to the applied field. At this angle we expect the sample area that is near the turns of the meanderline to be excited. By the same argument, when the in-plane angle is ±90° we expect the greatest coupling to FMR because a larger area

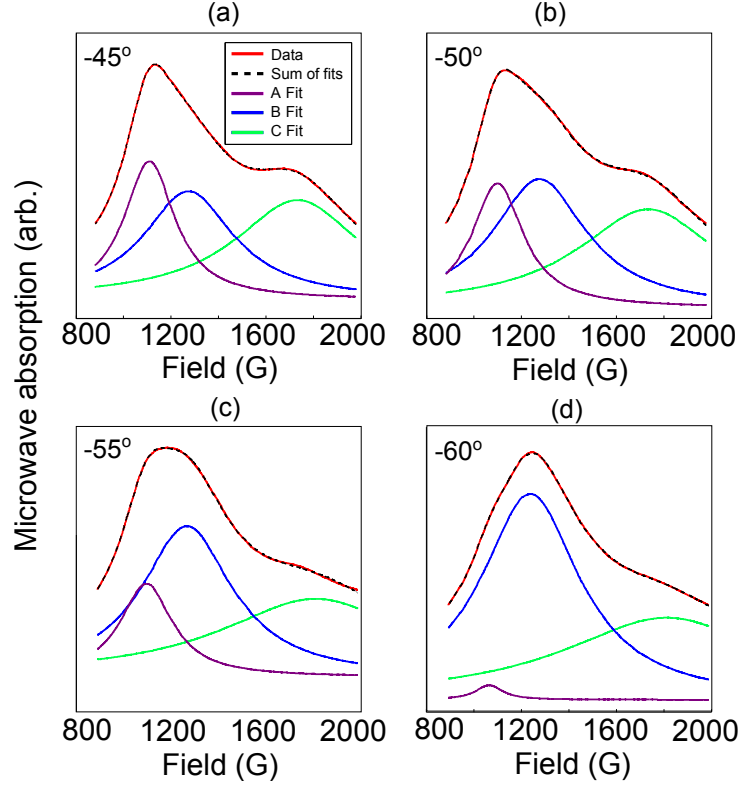Figure 2. (a) - (d) show the integrated FMR spectrum at -45°, -50°, -55° and -60° as a red line each. The blue green and pink curves are the fitted contributions of the **A**, **B** and **C** peaks. The sum of the fits, which is essentially indistinguishable from the data, denoted as a dashed black line. Notice how the amplitude of the **B** peak rises relative to the **A** peak at -60°.

of the sample is excited. Because the sample's physical properties and geometry are uniform over a area much larger than the footprint of the meanderline we do not expect the meanderline to excite different types of modes if the orientation relative to the sample is changed; only the surface area excited should change. Additionally, the microwave field generated by the meanderline is periodic on a one millimeter length scale, which is much longer than the colloidal crystal periodicity. Therefore, we expect to excite modes with a wave vector near $k = 0$. As the periodic topography of our system will endow magnetization dynamics with a spin wave band strucure, any modes that we excite should be k = 0 modes at the Γ point in the first Brillouin zone.

Fig. 2 depicts integrated spectra obtained experimentally at a microwave frequency of 10 GHz. We resolve three distinct modes centered around 1050, 1200, and 1750 G that we respectively name **A**, **B**, and **C**. For a uniform film the resonance field would be expected to lie just below 1100 G. This suggests that the modes are modifications of the uniform precession mode (the Kittel mode) caused by topography-induced demagnetization. We also rotate the in-plane field angle to study the influence of the underlying six-fold symmetry. Some examples of FMR spectra for in-plane field angles between -45° and -60° that represent the observed are shown in Fig. 2 (a) - (d). The **A**, **B**, and **C** modes are extracted by fitting the spectra to a superposition of Lorentzian functions. We will focus our current discussion on the **A** and **B** modes.

4

The field positions of these modes over a 180° range are shown in Fig. 3 (a) as blue circles. The individual branches are clearly independent from one another but there is an observed two-fold symmetry in the field angles. We believe this two-fold dependence to be artificially induced from shrinking that occurs in the spheres during drying following deposition. From SEM results (see supplemental) an approximate 5 % variation is measured in the diameter of the spheres. To remove this artificial effect we fit a $\cos^2(\theta)$ function to the field positions, shown as red solid lines in Fig. 3 (a). Subtracting this from the field positions yields the result in Fig. 3 (b). It is important to note that these two branches appear to be independent. In Fig. 3 (c) we plot the ratio of the intensities of the **A** and **B** modes to illustrate a very strong effect that is seen in Fig. 2. The effect is a six-fold dependence in the ratio of the intensity of **B** to the intensity of **A** with maxima in this ratio at $-60°$, $0°$, and $+60°$; a mechanism behind this observation, a suppression of the intensity of **A**, is described in the simulation results. Note that the maximum of the **B** to **A** ratio at $0°$ is attenuated compared to the ratio at $\pm60°$; we believe this to be caused by the sphere asymmetry that attenuates the amplitudes of **both** the **A** and **B** mode at $0°$. The origin of the **C** mode may be caused by demagnetized regions at defect edges. The high field and broad linewidth of the resonance is suggestive of a rough "edge" like boundary mode; this is further corroborated by the numerical simulations of defect-free systems where such a mode cannot easily be detected, although for some field angles there is a hint of a shoulder at about 8 GHz (in a field of 1000 G), which may indicate the existence of a mode localized to small regions in the unit cell. It should be mentioned that when fitting the spectra a constrained parameter search is used to avoid unphysical fitting situations. The error bands shown in Fig. 3 (c) are based on varying the limits of the upper and lower field range where the **A** mode and **B** mode are allowed to exist. The intrinsic error on the data points for a given constraint range is smaller than the data points.

To understand the microscopic origin of these resonances we performed micromagnetic simulations[13]. The simulation space consists of a 400×346.4 nm^2 area (XY plane) containing four unit cells of the underlying HCP polystyrene lattice. The total thickness of the simulated structure is 100 nm but with a topography approximating that of the Py film on the polystyrene colloidal crystal. The maximum height of the film at a given (x, y) coordinate is given by the height the Py film would have on top of the underlying spheres; in this way we create the topographically modified film having a centered hexagonal structure. The simulated $400 \times 346.4 \times 100$ nm^3 space including the Py film is discretized into $5 \times 3.4641 \times 5$ nm^3 tetragonal mesh with a magnetization director in each cell. Periodic boundary conditions were applied in the (x, y)-plane with 6×6 images included in the calculation of the magnetostatic fields. The static and dynamic magnetization is described by the Landau-Lifshitz-Gilbert equation

$$\frac{d\hat{m}(\mathbf{r}, t)}{dt} = -|\gamma_e|\hat{m}(\mathbf{r}, t) \times \mathbf{H}_{\text{eff}}(\mathbf{r}, t) - \frac{|\gamma_e|\alpha}{1 + \alpha^2}\hat{m}(\mathbf{r}, t) \times [\hat{m}(\mathbf{r}, t) \times \mathbf{H}_{\text{eff}}(\mathbf{r}, t)]. \tag{1}$$

Here, $\hat{m}(\mathbf{r}, t)$ is a unit vector along the local magnetization direction, γ_e is the electron gyromagnetic ratio,
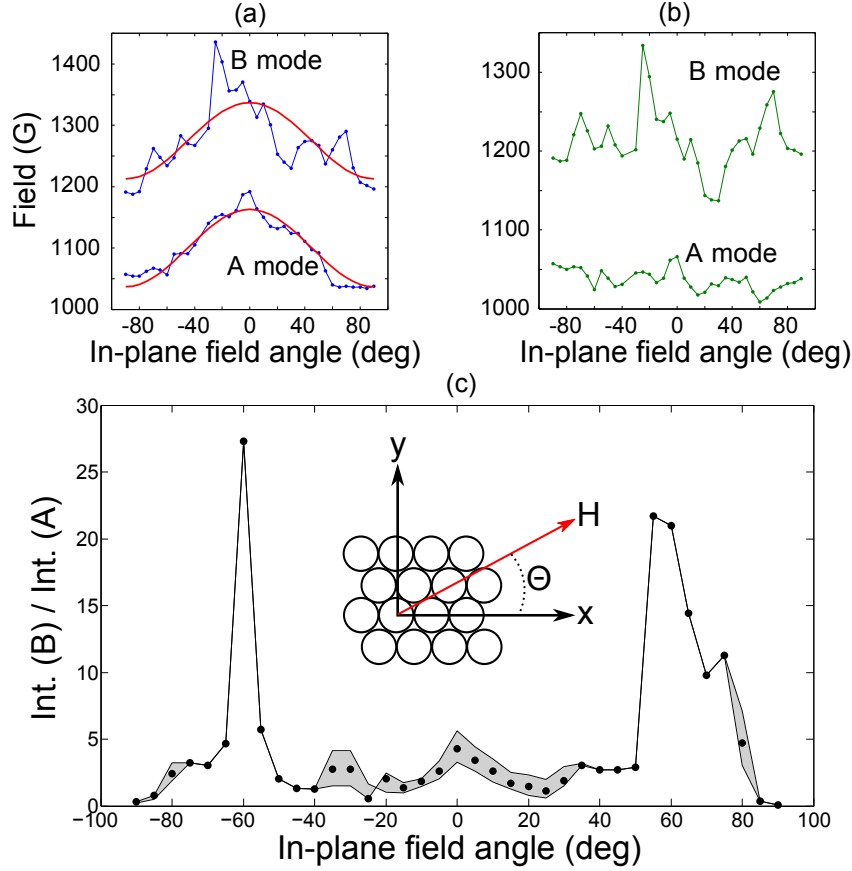
Figure 3. (a) shows the field dependence of both the **A** and **B** modes extracted from fitting. Aside from both branches being independent of one another there is an artificial two-fold angular dependence shown as the red line that is thought to arise from anisotropic sphere shrinkage. The remaining dependence after the anistropic part is removed is shown in (b). The six-fold dependent ratio of the **B** peak intensity to the **A** peak intensity is shown in (c).

here set to 2.95 GHz/kOe, α is the dimensionless damping set to 0.1 for static equilibration and 0.01 for the dynamic time-integration. The effective field $\mathbf{H}_{\mathrm{eff}}$ includes near-neighbor exchange (calculated using a six-point stencil in the parallel-epiped lattice), external field, and magnetostatic (demagnetizing) fields. An exchange coupling typical for Py of about 1.3 μerg/cm was used (the modes at or near the Γ point are rather insensitive to the exact value of the exchange coupling), and a zero-temperature saturation magnetization of 800 emu/cm^3. The system was first equilibrated with the larger damping for a given direction of the external field, using time steps of up to 2 ps. This equilibrium structure was then subjected to a uniform magnetic field for a duration of up to 0.5 ns after which the magnetization dynamics was integrated for 10 ns in timesteps of 250 fs using a modified Bulirsch-Stoer algorithm with error checking and adjustable timestep. The magnetostatic fields were calculated at each time step by multiplying the Fourier transformed instantaneous magnetization with the (stored) Fourier transformed demagnetizing tensor, and back-transforming to the space domain. We confirmed that our results were not dependent on the used mesh with a tetragonal symmety and that they obey a six-fold symmetry in the plane by performing similar numerical simulations with a $2.5 \times 3.4641 \times 2.5$ nm^3 tetragonal mesh on a numerical unit cell containing
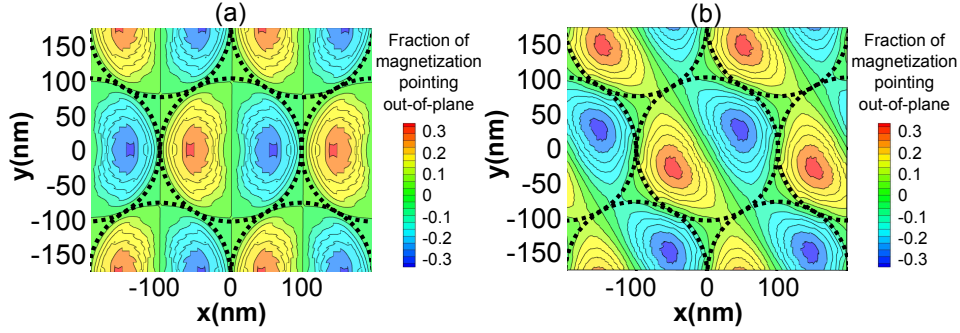
6

Figure 4. The simulated static configuration of magnetization is shown at 0° and 30° at (a) and (b) respectiviely. Specifically, we plot the fraction of the magnetization that is pointing out-of-plane. The largest tipping occurs where the magnetic field lines enter or exit an underlying colloid as indicated by the drawn in arrows. Here 30% of the magnetization can tip out of the plane.

two primitive unit cells of the system but with 7×7 periodic images for field angles of 15°, 25°, 30°, 40° 50°, and 60° degrees. In order to obtain results that can be directly compared to experimental spectra we average the entire magnetization of the nanostructure at each time step. This time-sequence can then be Fourier transformed to obtain a spectrum for each component of the magnetization. Additionally, in order to obtain spatially resolved information of the modes, we also collect the magnetization at a given (x, y) coordinate for each time step to create a time-sequence of 2D magnetization maps. This sequence is then Fourier transformed with respect to time to obtain a spatial map of the magnetization amplitude and phase at each frequency[14].

We also performed direct numerical diagonalization of the linearized LLG equation at field angles from 0° to 30° in steps of 5 degrees, and at 40°, 50°, and 60° degrees using a numerical unit cell containing two primitive unit cells of the system and with 7×7 periodic images, and a tetragonal mesh of size $5 \times 3.4641 \times 5$ nm^3 and a damping of zero. This alternative way to obtain resonant modes of ferromagnetic micro/nanostructures has been well described and implemented before[15,16]. For smaller field angles, the agreement between the numerical diagonalization and the time-integration is very good (we confirmed the slightly lower frequencies obtained from the time-integration is because of the finite damping; diagonalizing the linearized LLG equations with a finite damping of 0.01 pushed the frequencies down to the ones obtained by time-integration). For larger field angles $\gtrsim 20°$, the tetragonal lattice affects the numerical diagonalization and breaks the six-fold symmetry.

To illustrate the static configuration, we plot the out-of-plane fraction of the magnetization at a 0° and 30° in-plane field direction in Fig. 4. The in-plane component of the magnetization largely follows the applied field direction so that the only variation in the static configuration is an out-of-plane tipping that follows the curvature of the underlying colloid. The out-of-plane tipping is greatest in regions where the field is normal to a vector that is tangent to the circular perimeter of an underlying colloid. Unsurprisingly, when the field is parallel to this type of vector there is little out-of-plane tipping.
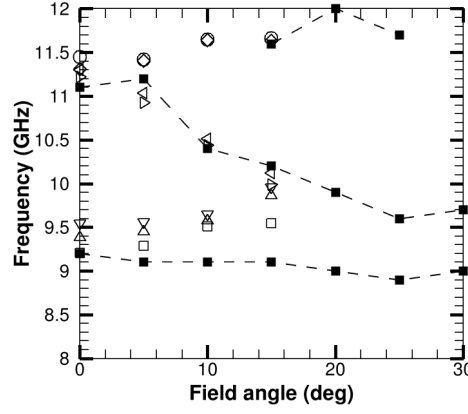
Figure 5. Modeled resonant frequencies obtained through numerical diagonalization (empty symbols) and numerical integration and Fourier transform (filled squares and dashed lines). Only the range $0° \leq \theta \leq 30°$ is displayed as the frequencies are symmetric about $\theta = 30°$.
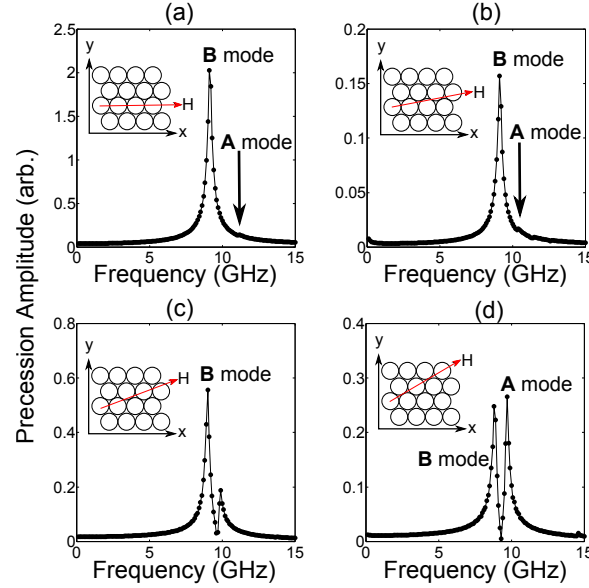

Figure 6. The simulated FMR spectra is shown at $0°$, $10°$, $20°$, and $30°$ in (a)-(d) respectively. The features that lie close in field-frequency space to the **A** and **B** mode are denoted. At $0°$ and $10°$ the **A** mode is weakly coupled to but higher energy non-spatially uniform modes are seen to exist.

The numerically obtained frequencies are shown as a function of field angle in Fig. 5, where the solid squares connected by dashed lines are the frequencies obtained from numerical time-integration, and the open symbols (squares, triangles, circles, and diamonds) are from numerical diagonalization (these latter are displayed only for field angles $\theta \leq 15°$ as the tetragonal lattice skewed the results for larger angles, as explained earlier). The numerical diagonalization yields a number of modes with odd symmetry in the unit cell along the field direction; these modes do not couple to the uniform field pulse. There is a band of three modes near 9.5 GHz that includes the Kittel-like nearly uniform mode that is excited by the uniform field pulse and obtained through numerical time-integration at about 9 GHz. There is also a band of higher-order modes with frequencies between 10 GHz and 11 GHz. One of the modes in this band

has has an even symmetry and couples to the uniform field pulse. Finally, there is a third band of modes close to 12 GHz, with a few of those coupling visibly to the uniform field pulse. The simulated spectra obtained thorugh numerical time-integration for field angles between 0° and 30° are shown in Fig. 6. It is clear that the higher-frequency peak couples very weakly to the uniform field pulse for field angles at 10° or smaller. The large peak found at all angles close to 9.0 GHz compares in field-frequency space to the experimentally observed **B** mode. We therefore identify the **B** mode as the Kittel-like near-uniform mode, and the higher-frequency band of modes as the **A** mode. We do not directly try to match the modes obtained from diagonalization with those obtained through time-integration; for the remainder of our discussion we shall focus on the two primary modes coupled to through the time integrated method.

To ascertain the topographical mode distributions of the **A** and **B** modes we plot amplitude and phase maps of each in Fig. 7 at an in-plane field angle of 30°. The lower energy **B** mode has large precession in the more heavily demagnetized regions of the spheres that lie along stripes passing midway between lattice sites (betwen the spherical caps), as seen in Fig. 7 (a). This region overlaps closely with where the out-of-plane tipping of the static configuration is nearly 30%. The precessional phase, shown in Fig. 7 (b), is seen to be uniform for this mode where the amplitude is large. In contrast, the **A** mode map depicted in Fig. 7 (c) has regions of large precession along stripes passing through the lattice sites (through the tops of spherical caps). Here the region of precession overlaps with regions of the sphere where the static configuration does not tip out-of-plane; this is consistent with the higher resonant frequency. The precessional phase for this running mode is also seen to be uniform [Fig. 7 (d)]. Furthermore, a mechanism for amplitude anisotropy and control can be surmised from analysis of the modes in Fig 7. The **A** mode amplitude is dramatically reduced at 0° and 10° where a continuous path that connects the precession amplitude from sphere to sphere is broken; we believe this is the mechanism responsible for the maxima in the ratio of amplitudes of modes **B** and **A** described earlier. Figure 8 shows precession and phase maps for the two main resonances predicted by simulations when the applied field is at 0°. Figure 8 (a) and (b), show the **B** mode profile,and Fig. 8 (c) and (d) show the precession and phase maps for the higher-frequency (at fixed field) **A** mode. As the field is rotated from 30° to 0°, the lines of maximum amplitude of the **A** mode, which connect the top of the spherical caps at 30°, now connect the top of one cap to the region between to neighboring caps, where the amplitude has broadened into three bands. This higher spatial variation in the magnetization distribution of the mode leads to a blue-shift in the frequency and pushes it up to 11.1 GHz.

Before concluding we must point out that the angular dispersion obtained by the numerical simulation is relatively flat for the **B** mode, while that of the **A** mode exhibits a more pronounced angular variation (Fig. 5). This is in contrast with the experimentally obtained angular dispersions, where that of the **A** is relative flat, while that of the **B** mode shows more angular variation. We believe that discrepancy originates in defects and imperfections of the colloidal crystal, which is underscored by the apparent lack of six-fold
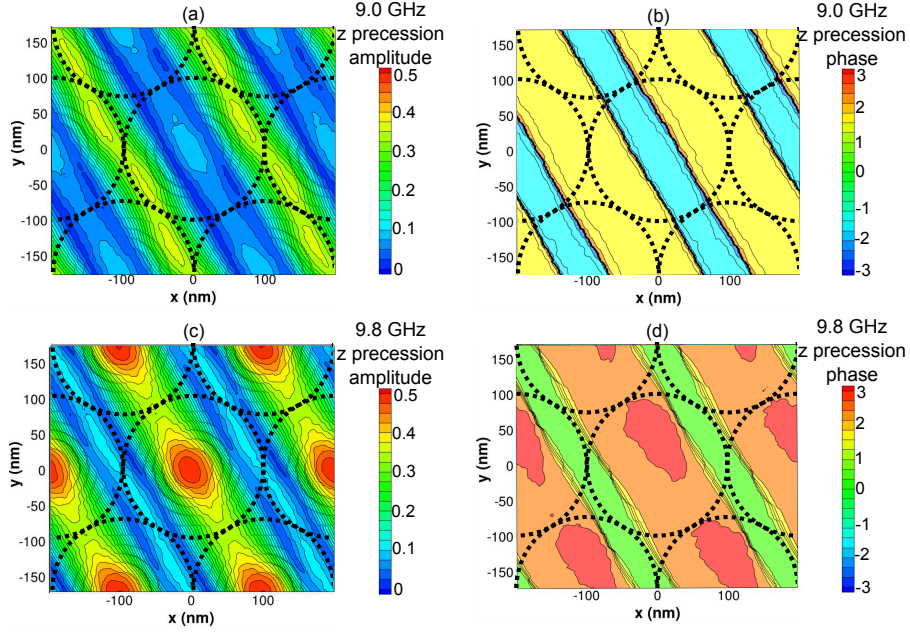
Figure 7. The microscopic details that distinguish the **A** mode from the **B** mode are best seen when the field is applied at 30°. In (a) and (b) we see the power map and phase map for the **B** mode while in (c) and (d) the same information is shown for the **A** mode.

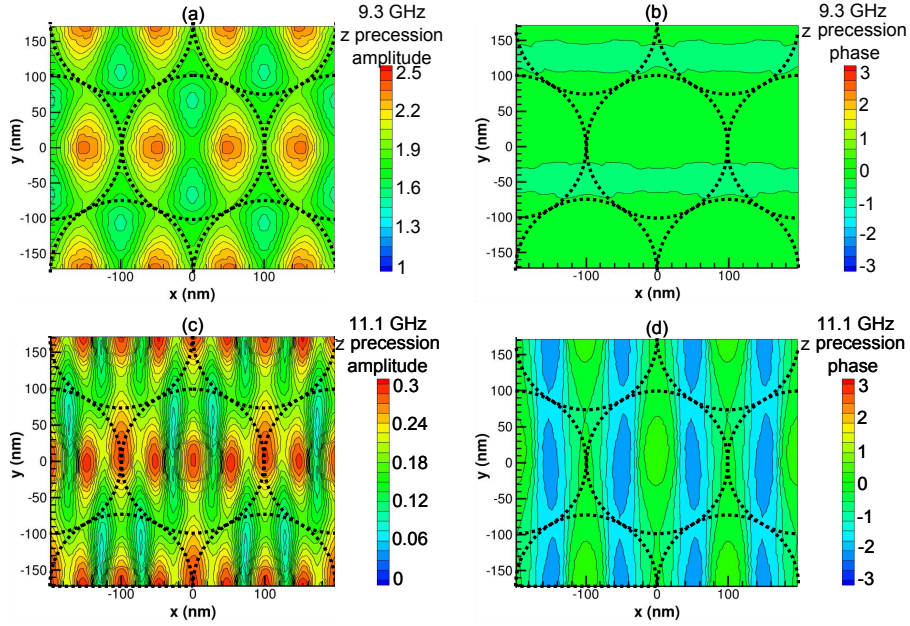Figure 8. Here we show the **A** and **B** modes at 0°. (a) and (b) show the amplitude and phase map for the **B** mode, which is a type of fundamental Kittel-like mode; (c) and (d) show the amplitude and phase information for the **A** mode.

symmetry in the experimental angular dispersions for the modes [Fig. 3 (b)]. Nevertheless, we are confident that we have correctly identified the modes based on the following three agreements between experimental and numerical results: 1) Both the **A** and **B** mode do not cross. 2) The separation in field/frequency space between the modes is in good qualitative agreement. 3) Most importantly, the sudden drop in coupling to the **A** mode relative to the **B** mode at 0° and ±60° is seen in both experiment and simulation.

In this work we have demonstrated the excitation of multiple $k = 0$ ferromagnetic resonance modes in a thin ferromagnetic film over a large area nanostructure that has a periodically modulated topography. The presence of multiple Γ point $k = 0$ modes indicates the existence of a spin wave band structure. We were able to continuously vary the topography due to an underlying six-fold symmetric colloidal crystal. Our method of generating new ferromagnet resonance modes is an alternative to traditional lithographical means. Experimental evidence through FMR spectra yields spectra that have a superposition of many modes. Through simulation, we have offered visualizations on the microscopic details that reveal two distinct fundamental modes residing in our system along with higher energy. From an exploratory viewpoint we find that our system underscores both the robustness and fragility of spin wave modes in nanostructures. Simulations show that **A** mode is highly anisotropic and hence fragile, while the **B** mode is considerably more robust. Experimental observations support the details of this conjecture.

---

[1] V. S. Bhat, J. Sklenar, B. Farmer, J. Woods, J. T. Hastings, S. J. Lee, J. B. Ketterson, and L. E. De Long, Phys. Rev. Lett. **111**, 077201 (2013).

[2] M. Krawczyk, D. Grundler, J. Phys.: Condens. Matter **26**, 123202 (2014).

[3] V. Novosad, F. Y. Fradin, P. E. Roy, K. S. Buchanan, K. Yu. Guslienko, and S. D. Bader, Phys. Rev. B **72**, 024455 (2005).

[4] B. Van Waeyenberge, A. Puzic, H. Stoll, K. W. Chou, T. Tyliszczak, R. Hertel, M. Fähnle, H. Brückl, K. Rott, G. Reiss, I. Neudecker, D. Weiss, C. H. Back, and G. Schütz, *et al.*, Nature **444**, 461 (2006).

[5] S. Gliga, A. Kákay, R. Hertel, and O. Heinonen, Phys. Rev. Lett. **110**, 117205 (2013).

[6] M. V. Sapozhnikov, S. A. Gusev, B. B. Troitskii, and L. V. Khokhlova, Opt. Lett. **36**, 4197 (2011).

[7] M. V. Sapozhnikov, O. L. Ermolaeva, B. G. Gribkov, I. M. Nefedov, I. R. Karetnikova, S. A. Gusev, V. V. Rogov, B. B. Troitskii, and L. V. Khokhlova, Phys. Rev. B **85**, 054402 (2012).

[8] R. Streubel, D. Makarov, F. Kronast, V. Kravchuk, M. Albrecht, and O. G. Schmidt, Phys. Rev. B **85**, 174429 (2012).

[9] D. Mitin, D. Nissen, P. Schädlich, S. S. P. K. Arekapudi, and M. Albrecht, Jour. Of App. Phys. **115**, 063906 (2014).

[10] M. Kostylev, A. A. Stashkevich, Y. Roussigné, N. A. Grigoryeva, A. A. Mistonov, D. Menzel, N. A. Sapoletova, K. S. Napolskii, A. A. Eliseec, A. V. Lukashin, S. V. Grigoriev, and S. N. Samarin, Phys. Rev. B **86**, 184431 (2012).

[11] P. Jiang, J. F. Bertone, K. S. Hwang, and V. L. Colvin, V. L., Chem. Mater. **11**, 2132 (1999).

[12] C. C. Tsai, J. Choi, S. Cho, S. J. Lee, B. K. Sarma, C. Thompson, O. Chernyashevskyy, I. Nevirkovets, and J. B. Ketterson, Rev. Sci. Instrum. **80**, 023904 (2009).

[13] D. Schreiber, O. Heinonen, and A.K. Petford-Long, Phys. Rev. B **80**, 014411 (2009).

[14] J. Sklenar, V. S. Bhat, L. E. DeLong, O. Heinonen, and J. B. Ketterson, Appl. Phys. Lett. **102**, 152412 (2013).

[15] P.K. Muduli, O. Heinonen, and J. Åkerman, Phys. Rev B **83**, 184410 (2011).

[16] K. Rivkin and J. B. Ketterson, J. Magn. Magn. Mater. **306**, 204 (2006).